Solid and 3D beam finite element models for the nonlinear elastic analysis of helical strands within a computational homogenization framework

Fabien Ménard, Patrice Cartraud

To cite this version:

Fabien Ménard, Patrice Cartraud. Solid and 3D beam finite element models for the nonlinear elastic analysis of helical strands within a computational homogenization framework. Computers & Structures, 2021, 257, pp.106675. 10.1016/j.compstruc.2021.106675 . hal-04667460

Solid and 3D beam finite element models for the nonlinear elastic analysis of helical strands within a computational homogenization framework

Fabien Ménard, Patrice Cartraud

Institut de Recherche en Génie civil et Mécanique (GeM), UMR CNRS 6183 Ecole Centrale de Nantes, BP 92101, 44321 Nantes cédex 3, France

---

Abstract

This paper proposes a computational approach for studying the overall behaviour and local stress state of strand-type structures. This method is based on the homogenization theory of periodic beamlike structures, with the local problem posed on the strand axial period being solved using the finite element method. This approach fully utilises the strand's helical symmetry, thus minimising the size of the computational domain. Consequently, accounting for geometric complexity and contact interactions, which are of paramount importance for bending loads, is more straightforward. The numerical model mesh size can also be reduced thanks to the use of beam elements, and one objective of this paper is to assess the accuracy of such a model in comparison with solid element models and analytical results. These comparisons are performed on both single-layer and multi-layer strands. Results demonstrate the capability of the proposed computational approach to accurately capture the nonlinear bending behaviour stemming from the stick-slip transition as well as local stress distributions. As for the beam model, it apparently offers a very good compromise between accuracy and numerical efficiency.

Keywords: Homogenization, Helical symmetry, Strand, Cable, Bending, Contact, Finite element method

---

1. Introduction

Metal cables are widely used in various industrial fields due to their high tensile strength relative to bending stiffness. Applications extend from electrical power given their ability to transmit electrical current to civil engineering structures like bridges or anchored retaining walls. The components of metal cables commonly consist of an arrangement of helically-wound wires, in creating strands from an assembly of several layers of wires. The cable cross-section can be quite complex, with strand arrangements possibly involving simple and double helical paths, or simpler featuring a single straight strand, as is the case for the cables considered in this work.

Strand structural analysis raises modelling challenges due to the geometric complexity and nonlinearities resulting from friction between components, especially for a bending load.

Given the objective of a service life design of these structures, it is therefore necessary to be able to accurately predict the overall behaviour and local stress state within the strand.

Strand behaviour can be studied by means of analytical approaches, in modelling individual components as curved beams and introducing some approximations and assumptions. In [1], a nonlinear formulation was established to take into account the radial contraction of the various components due to the Poisson effect. This formulation has been linearised in the single-layer strand case (see [2]). A concise formulation has been proposed in [3] that takes into account the stiffness matrix symmetry. A more recent model incorporating both radial contraction of the wires due to the Poisson effect and wire flattening effects was proposed in [4]. Most of the works dedicated to analytical models have been focused on the axial cable behaviour, while an interesting loading case is obtained when combining a tensile force with bending. Depending on the stress state within the cable, the contact between its components can be in either a stick or slip state, which leads to nonlinear bending stiffness. Such a consideration has been factored into the models proposed by Papailiou [5] and Foti [6], in which a nonlinear transition state is defined between the stick and slip states. Some analytical formulations provide stress estimations within wires for axial-torsional loads [1] as well as for bending with an initial tensile load [5]. However, addressing all mechanical and contact issues in an analytical formulation can prove to be cumbersome, especially when the strand cross-section is composed of many layers.

Over the last twenty years, several authors have developed numerical models that consider geometric complexity and contact interactions. Single-layer strands have been studied with solid finite element models in the cases of axial loading [7], pure bending [8] and tension-bending loading [9] and [10]. Multi-layer strands have been considered in [11], [12] and [13]. The inclusion of contact interactions significantly increases computation time, especially when solid elements are being used. One way to reduce the computational cost is to use beam models. In [14], [15], [16] and [17], a small sliding assumption between strand components has been adopted, in turn leading to a low computation time. Contact resolution is done by a node to node approach using contact elements between strand layers. A finite sliding has been assumed in [18], [19] and [20] where contacts are solved by a beam-to-beam algorithm firstly developed in [21]. Another approach to decreasing the computational cost calls for taking advantage of helical symmetry in order to reduce the structural analysis to just a small portion of the cable. If the loading also fulfils helical symmetry, then a 2D model is an eligible option, as performed in [22] and [23] to study the axial behaviour of single strands. However, once bending is considered, a 3D model is required, e.g. [8].

The main objective of this work is to propose a computational approach based on the periodic homogenization method developed in [24] involving this time contact nonlinearities. The size of the computational domain is thus reduced to an axial strand period using specific periodic boundary conditions. In addition, two types of finite element models featuring solid and beam elements will be studied in order to compare the numerical results for axial, torsional and bending loadings. These comparisons will be drawn on the overall strand behaviour and local stress distributions, in focusing on bending with an initial tensile load. To validate the method, both single-and multi-layer strands will be examined and the results compared to the literature.

2. Description of the mechanical problem

2.1. Multi-layer strand geometry

The strand geometry considered herein consists of m concentric wire layers and a central core, comprising respectively a helical and rectilinear mean line, see Figure 1a, with the layers being wound around each other. In most strands, the winding angle on two successive layers has opposite signs. Each layer j is defined by: its number of wires n_j, the wire radius R_{sj}, the mean layer radius R_{hj}, and its lay angle α_j. The core of the strand is defined by its radius, denoted R_c, see Figure 1b.

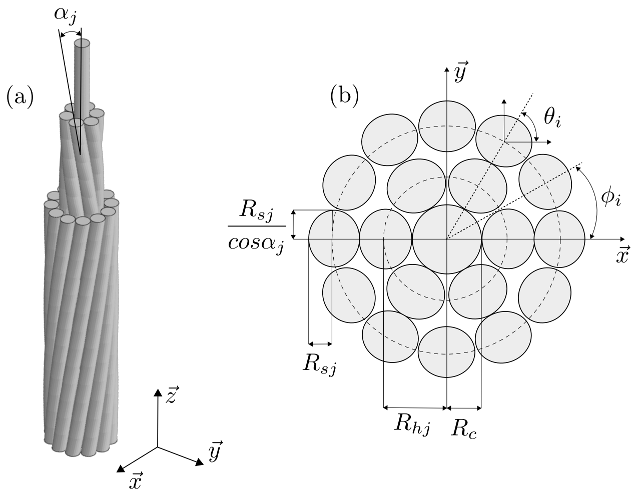

Figure 1: Representation over the length (a) and cross-section (b) of a strand composed of two layers and a core

The helix pitch length of a layer j, denoted p_j, is determined according to both the lay angle and mean layer radius, such that:

$$p_j = \frac{2\pi R_{sj}}{tan(\alpha_j)}. \tag{1}$$

As detailed in [18] and [25] for a z-axis strand, the mean line of a wire i belonging to a layer j can be defined by the following parametric equations:

$$x_{ij} = R_{hj} cos\left(\phi_i + \frac{2\pi(i-1)}{n_j} + \frac{tan(\alpha_j)p_j}{R_{hj}}t\right), \tag{2}$$

$$y_{ij} = R_{hj} sin\left(\phi_i + \frac{2\pi(i-1)}{n_j} + \frac{tan(\alpha_j)p_j}{R_{hj}}t\right), \tag{3}$$

$$z_j = p_j t, \tag{4}$$

with $t \in [0, 1]$ and ϕ_i being the initial angular position of the wire in the strand section, see Figure 1b.

2.2. Contact interactions within a multi-layer strand

During operations, various contact interactions appear between the strand components, see Figure 2a, namely [7]:

- Intra-layer contacts involving a circumferential normal: contacts between wires of the same layer established along contact lines, see Figure 2b.
- Inter-layer contacts involving a radial normal: contact between wires of two successive layers. In the non-deformed state, these contacts can be considered as contact points, see Figure 2c, i.e. in the case of overlapping layers. They are established along contact lines in the case of contact between layer and core.

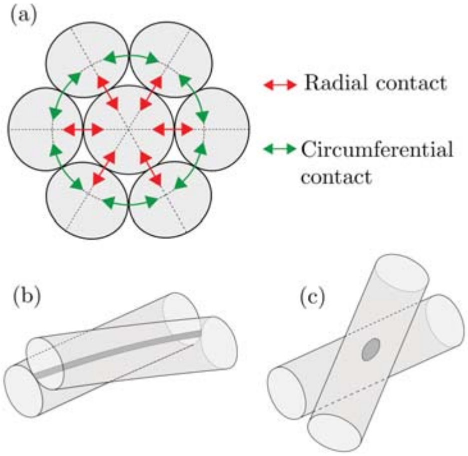

Figure 2: Representation of possible contact interactions within a strand section: radial and circumferential contact (a); contact line (b); and a contact point (c)

Depending on the pressure present between layers, the contact plays an important role, in particular in the case of bending. Significant contact forces will in fact tend to stiffen the structure. Conversely, for low intensities, the contact forces are negligible and allow for relative displacement between components. Contact interactions therefore have a major influence in the study of strand behaviour.

Contact problems are solved within the framework of general contact theory, according to which normal contact is translated under the conditions of Hertz-Signorini and tangential contact is approximated by Coulomb's Law with friction coefficient μ, [26].

The relative sliding of strand wires varies depending on their angular position in the section [27]. For bending loading, the first wire in a slip state occurs for the closest wire to the bending axis on the outer layer. Subsequently, adjacent wires of the same layer also slip. This phenomenon evolves from the outer layer to the inner layer until reaching a full slip.

The longitudinal slip u of a strand wire i in layer j in pure bending can be approximated analytically by means of a loxodromic curve, such that:

$$u = R_{hj}^2 \frac{cos^2\alpha_j}{sin\alpha_j} \kappa cos\phi_i, \tag{5}$$

where κ is the strand curvature.

It is important to note that in certain cases, the manufacturing process or loading intensity generates spaces between wires of the same layer or between wires of two adjacent layers, see [4] and [28]. Under these circumstances, the contact surfaces can be heterogeneous between layers or within a layer, thus modifying the final behaviour and sliding state of the strand. In this work however, the initial deformations tied to the manufacturing process are not taken into account, and a homogeneous contact is assumed.

2.3. Homogenization method for periodic beams

The homogenization method has already been employed in the past for strand or periodic beam like structures ([24], [29], [30], [31], [32] and [33]). This method offers an efficient and rigorous means for reducing the size of the Boundary Value Problem (BVP) domain, thanks to the structural axial periodicity, which stems from the helical geometry of cable components.

This method is suitable for the case of helical wire assembly, whereby the helix axis is parallel to the slenderness direction or is itself a helix. The helical structure is then considered as a slender 3D structure, with geometric heterogeneities repeating periodically along its main axis, see Figure 3.

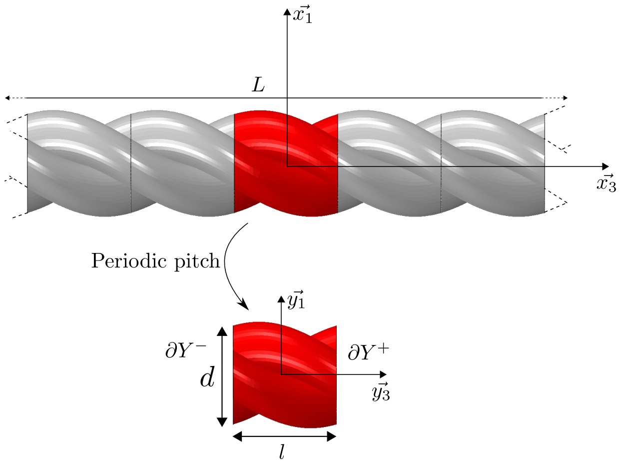

Figure 3: Strand representation with a periodic structure

In the case of a helical strand, the period is defined by the helical symmetry of the layer. The axial period l_j of layer j is obtained by dividing the pitch, (1), by the number of wires n_j in the layer, such that:

$$l_j = \frac{p_j}{n_j}. \tag{6}$$

An example of a period is presented in Figure 3 for a 3-wire strand: $n_j = 3$. In order to determine the length l of the axial strand period with several layers, a common period between layers must first be defined, i.e.:

$$l = k_j \frac{p_j}{n_j} = k_{j+1} \frac{p_{j+1}}{n_{j+1}} = ... = k_m \frac{p_m}{n_m}, \tag{7}$$

with $k_j \in \mathbb{N}$.

This homogenization approach is based on the asymptotic expansion method, in taking into account that the initial 3D problem, posed on the cable structure, involves two small parameters, defined as: 1) the ratio of the size of the axial period to the cable length, and 2) the inverse of the cable slenderness. The latter parameter is also the ratio of cable diameter to cable length. Without any restrictions imposed, these two parameters can be considered equal and are denoted ϵ:

$$\epsilon \simeq \frac{l}{L} \simeq \frac{d}{L}. \tag{8}$$

A microscopic scale y can now be introduced such that $y = x/\epsilon$.

The asymptotic expansion method consists of searching for the displacement solution to the initial 3D problem in the form of an expansion in increasing powers of ϵ. The initial 3D problem is then decomposed into a series of microscopic 3D problems, posed on the cable axial period, as well as a series of macroscopic 1D problems, see [31], [32] and [33]. The lower-order macroscopic 1D problem is a Navier-Euler-Bernoulli-Saint-Venant beam problem, with a homogenised behaviour obtained from the solution to the microscopic problem. This problem can be expressed as follows, with more details available in [24]: Find the displacement field y_3 periodic u^{per}, strain ε and stress σ from the macroscopic strain state corresponding to extension E^E, curvatures E^{F_α}, with $\alpha = [1, 2]$, and torsion rate E^T, such that:

$$\left\{ \begin{array}{l} div_y \sigma = 0, \\ \sigma = a(y) : e, \\ e_{\alpha\beta} = e_{y_{\alpha\beta}}(u^{per}), [\alpha, \beta] = [1, 2], \\ e_{13} = e_{y_{13}}(u^{per}) - y_2 E^T/2, \\ e_{23} = e_{y_{23}}(u^{per}) + y_1 E^T/2, \\ e_{33} = e_{y_{33}}(u^{per}) + E^E - y_\alpha E^{F_\alpha}, \\ \sigma.n = 0 \text{ on } \partial Y, \\ u^{per} \text{ periodic and } \sigma.n \text{ anti-periodic}, \end{array} \right. \tag{9}$$

where a is the elastic modulus, and div_y and e_y the equilibrium and strain operators at the microscopic scale. Periodic signifies l-periodic in variable y_3, while anti-periodic means that $\sigma.n$ are opposite on opposite sides ∂Y^+ and ∂Y^- in the strand axis direction. Microscopic problems with imposed macro-deformations (9) are solved using the finite element method with specific periodic boundary conditions.

As explained previously, the lower-order macroscopic problem is a 1D beam problem. This problem is derived from compatibility conditions which express that microscopic problems admit a solution. These conditions lead to a lower-order macroscopic problem which turns out to be a beam problem involving internal forces which are the macroscopic axial force N, the macroscopic bending moments M_α, as well as the macroscopic torsional moment M_3. They are defined by both integrating microscopic stresses over the strand section and averaging on the period length, i.e. [24]:

$$\begin{cases} N(x_3) = \langle \sigma_{33} \rangle, \\ M_\alpha(x_3) = \langle -y_\alpha \sigma_{33} \rangle, \\ M_3(x_3) = \langle -y_2\sigma_{13} + y_1\sigma_{23} \rangle, \\ \langle . \rangle = \dfrac{1}{l} \int_Y .dy_1 dy_2 dy_3. \end{cases} \tag{10}$$

The strain variables of this 1D macroscopic problem are the macroscopic strains E^E, E^{F_1}, E^{F_2} and E^T introduced previously. Thus, from the solution of the microscopic problem (9), the homogenised behaviour can thus be written in the following form:

$$\begin{Bmatrix} N \\ M_1 \\ M_2 \\ M_3 \end{Bmatrix} = \left[a^{hom}\right] \begin{Bmatrix} E^E \\ E^{F_1} \\ E^{F_2} \\ E^T \end{Bmatrix}, \tag{11}$$

where $[a^{hom}]$ defines the homogenised stiffness matrix. Each column of the homogenised stiffness is obtained from the solution of microscopic problem (9), considering four elementary macroscopic strain states with only one non zero component of the macroscopic strain $\{E^E, E^{F_1}, E^{F_2}, E^T\}$.

The mathematical framework of the homogenization method is well established for perfectly bonded components, for which convergence results are available, see e.g. [32]. Its extension to a structure comprising several components with contact interactions is questionable. In order to investigate this question, the microscopic problem (9) with periodic boundary conditions have been solved for the axial period, but also for larger domains built with three or five axial periods. For the most critical bending loading considered in the study regarding the amplitude of the longitudinal slip, it has been found that the homogenised behaviour was not sensitive to the size of the domain, since the deviation between results of one and five axial periods is about 0.1 %. Moreover the local stress state obtained from the solution of the microscopic problem on one axial period exhibits only negligible departure from that obtained on the central axial period of larger domains. These results therefore justify the extension of the classical framework of homogenisation theory to the case of periodic structure with non-linear contact.

3. Finite element models

The helical strand study is presented here through three finite element analyses based on models with solid or beam elements. The ABAQUS software has been used as an FEA solver within the framework of linear elasticity and in considering small displacements and small deformations. Moreover, the finite element solution takes contact nonlinearities into account. The assumptions and construction of the relevant finite element models indicate how to solve problems resulting from the homogenization method on a strand period.

3.1. Geometry and meshing

The geometry and mesh for these finite element models are generated using in-house software developed in MATLAB. The strand period length used for modelling is defined by equation (7). The coordinate system, correlated with the period, is such that the main strand axis coincides with $\vec{y_3}$-axis, whereby the origin lies at the strand centre, see Figure 4.

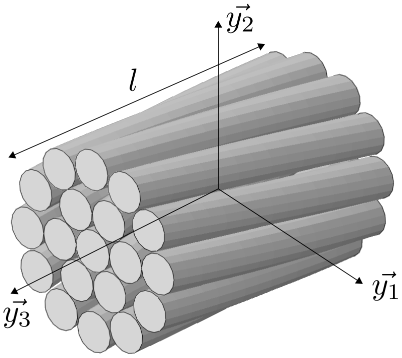

Figure 4: Depiction of the strand period, composed of two layers with: $l = \dfrac{p_1}{n_1} = \dfrac{p_2}{n_2}$

Solid element model

In the case of a finite element model using solid elements, the first step consists of building a wire section mesh with quadrangle elements in the plane ($\vec{y_1}$,$\vec{y_2}$). By neglecting the initial deformations, which may be due to the manufacturing process, the layer wire section can be approximated, in ($\vec{y_1}$, $\vec{y_2}$), by an elliptical section while the core section is circular, see Figure 5a. Subsequently, the mean wire line is defined using equations (2), (3) and (4). The wire section mesh is then translated along the mean component line by applying a translation defined by means of the axial discretisation and a rotation θ in order to orient the wire section radius according to the strand section radius, see Figure 5b. Treatment of the contact by the finite element method is highly dependent on both the axial and circumferential discretisation of each wire. The number of finite elements should thus be sufficiently large to obtain a good representation of the contact surface and reduce the geometric discontinuities. This last step entails building a connectivity table that allows creating a 3D mesh of hexahedral elements, C3D8 in ABAQUS, see Figure 5c. The material properties are defined in the elastic domain, as characterised by Young's modulus E and Poisson's ratio ν.

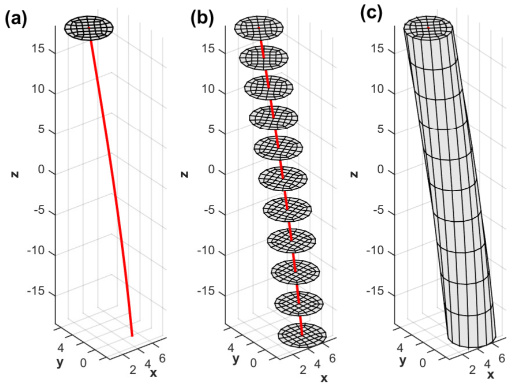

Figure 5: Generation of the mesh of a helical wire composed of solid elements: (a) generation of the mean line and surface mesh, (b) translation and rotation of the surface mesh along the mean line, and (c) building of the 3D mesh

Beam element model

For the finite element model composed of beam elements, the mesh is directly generated from equations (2), (3) and (4). The cross-section perpendicular to the mean wire line is defined in ABAQUS as being circular with radius R_{sj} for a layer wire and R_c for the central core. Timoshenko beam elements are used to account for shear forces resulting from contact interaction. The material properties are defined in the elastic domain, as characterised by Young's modulus E and Poisson's ratio ν.

3.2. Contact modelling

For the normal contact solution of the two models presented herein with either solid or beam elements, linear penalisation method is used because of the large number of contact involved in order to reduce computational time. Two methods were preliminary studied in order to determine the penalty stiffness in the normal direction. One can use Hertz theory [34] as mentioned in [14]. The second method consists to scale the representative underlying element stiffness in contact as used in Abaqus, see [35]. The penalty stiffness increases linearly from the initial penalty stiffness, equal to the representative underlying element stiffness, to the final penalty stiffness evaluated at 10 times the initial penalty stiffness. A comparison between those two methods in terms of contacts penetration, homogenised stiffness and numerical convergence showed no significant deviation. Thus, the software method is retained thereafter.

Tangential contact resolution is also performed based on the penalty method in regularising Coulomb's Law, see Figure 6. The contact tangential stress σ_T, proportional to displacements, can be written at increment i as follows:

$$\sigma_{T_i} = \sigma_{T_{i-1}} + \frac{\mu\sigma_N}{\gamma^{crit}}\gamma_i, \tag{12}$$

where γ^{crit} is the critical relative displacement between the components in contact, in delineating the stick behaviour and slip behaviour. This expression is defined as a fraction of the characteristic length l_e of the element surface in contact:

$$\gamma^{crit} = \beta l_e. \tag{13}$$

The value of β must be defined by the user. The choice of a low parameter β will tend to generate more flexible behaviour, by decreasing the transition threshold from the slip-to-stick state. In the case of a large parameter, Coulomb's Law will be better approximated but may cause convergence problems.

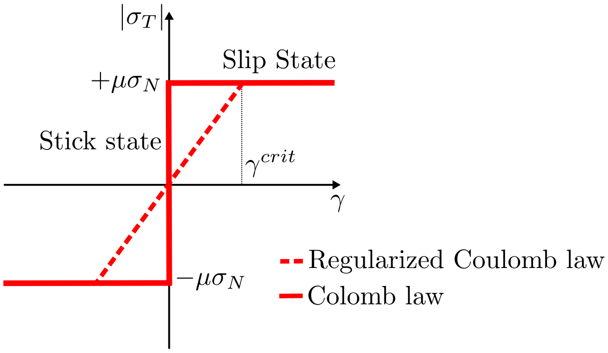

Figure 6: Tangential contact resolution with the penalty method in regularising Coulomb's Law from critical relative displacement γ^{crit}

Contact algorithm for solid elements

The type of contact interactions differs depending on which model is being considered. When taking strand geometry into account, a node-surface algorithm is chosen to solve contact problems for solid elements. In addition, this approach enables reducing model size and considerably simplifying the mesh, which avoids mesh matching at the contact interface.

Contact algorithms for beam elements

The beam-to-beam contact modelling is widely studied in the literature, see for example [19], [21] [36] and [37] which provide developpments that are contained in the proposed commercial code. Beam-to-beam contact can be used in the case of a helical strand, e.g. [18] and [16]. Beam element nodes are located on the mean line, while the contact is established on the section boundary. An initial formulation of the beam-to-beam contact, called cross formulation, serves to solve the contact point problem by projecting the contact point onto the beam elements, see Figure 7a. The radial formulation of the beam-to-beam contact is used in the case of a contact line where contact conditions are evaluated in each node, see Figure 7b. For this latter formulation, it is necessary to generate one additional node at each section in contact. Combining these two formulations resolves all types of contact present in a multi-layer strand under the small displacements assumption and with a regular mesh. However, it has been shown in [38] that beam-to-beam contact is time-consuming for a multi-layer strand, and moreover convergence is elusive especially for a bending load.

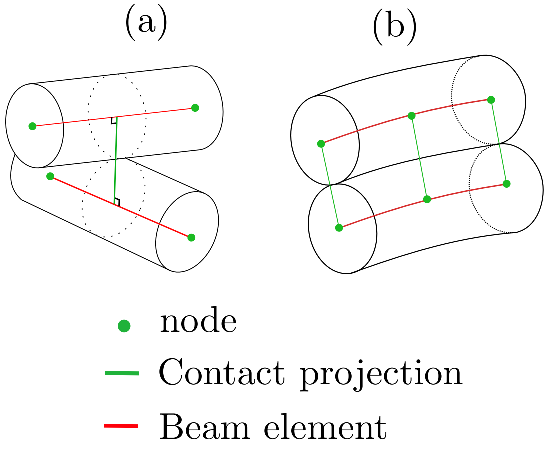

Figure 7: Contact formulation for beam-to-beam contact: (a) cross formulation, and (b) radial formulation

A second approach, inspired by the work reported in [38], is developed here to solve contact problems with beam elements. The cross-section boundary of the beam elements has been discretised using 4-node surface elements called SFM3D4 in ABAQUS. This surface is solely dedicated to the contact and has neither stiffness nor thickness. In order to link the contact surface with the beam, each node of the surface is rigidly constrained to the displacement (by translation and rotation) of its projection node on the beam element. The connection is carried out using a rigid beam (”Multipoint constraints”), see Figure 8. The contact area discretisation is performed with a node-surface algorithm. Since contact surfaces have no stiffness, it is necessary to combine the penalty method with the Lagrangian method in order to limit contact surface penetration and define the contact stiffness. A fine discretisation of the contact zone can be conducted using this approach without increasing computation time.

It is important to note that the contact between beam elements assumes a constant radius section, making it impossible to account for section contraction due to the Poisson's effect and section deformation due to contact forces, see [18].

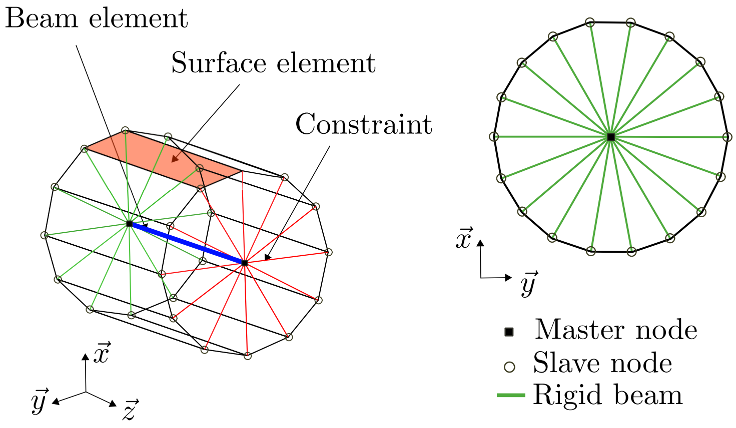

Figure 8: Connection between surface elements and beam elements using rigid beam elements

Contact tracking approaches

Regarding the slip between the various strand component, one can adopt small sliding assumption as in [14], [15] and [16]. Contrary to finite sliding approach, with small sliding method the contact relationships are established just once, at the beginning of the analysis, thus leading to computational savings. However, small sliding tracking approach is not available for beam-to-beam formulation and one objective of this paper is to compare the numerical results obtained from different finite element models. Therefore, although finite sliding tracking approach increases the calculation times, this method will be used in the following.

3.3. Boundary conditions

Microscopic problems (9) are solved using the finite element method, with implementation being based on introducing additional nodes whose degrees of freedom are the macroscopic strains, see [39] and [40]. Other methods can also be employed, see e.g. [41]. In our case the finite element solution corresponds to the total displacement field $\vec{u}$, i.e. the sum of a periodic displacement field denoted $\vec{u}^{per}$ and a displacement field related to the macroscopic strains. It can be defined as:

$$\begin{cases} u_1 = u_1^{per} + \frac{1}{2} y_3^2 E^{F_1} - y_2 y_3 E^T, \\ u_2 = u_2^{per} + \frac{1}{2} y_3^2 E^{F_2} + y_1 y_3 E^T, \\ u_3 = u_3^{per} + y_3 E^E - y_\alpha y_3 E^{F_\alpha} \quad , \quad \alpha = [1,2]. \end{cases} \tag{14}$$

The periodic boundary conditions on u^{per} are taken into account through linear relations, in connecting each degree of freedom of two opposite nodes belonging to the boundary ∂Y^+ and ∂Y^- in the axial strand direction, see Figure 3.

In the case of solid elements, the translational degrees of freedom of the boundaries ∂Y^+ and ∂Y^-, denoted U_i^+ and U_i^-, are linked by the following equations [24]:

$$U_1^+ - U_1^- = l(\overline{y}_3 E^{F_1} - y_2 E^T), \tag{15}$$

$$U_2^+ - U_2^- = l(\overline{y}_3 E^{F_2} + y_1 E^T), \tag{16}$$

$$U_3^+ - U_3^- = l(E^E - y_\alpha E^{F_\alpha}), \quad \alpha = [1,2], \tag{17}$$

with $\overline{y}_3 = \frac{1}{2}(y_3^+ + y_3^-)$ and $y_\alpha = y_\alpha^+ = y_\alpha^-$.

In the case of beam elements, three other equations apply for the rotational degrees of freedom of the boundaries ∂Y^+ and ∂Y^-, denoted θ_i^+ and θ_i^- [42]:

$$\theta_1^+ - \theta_1^- = l E^{F_1}, \tag{18}$$

$$\theta_2^+ - \theta_2^- = l E^{F_2}, \tag{19}$$

$$\theta_3^+ - \theta_3^- = l E^T. \tag{20}$$

In order to calculate the solution to problem (9) for an arbitrary macroscopic strain, two reference nodes A and B are created with respectively one and three degrees of freedom: $A = \left\{E^E\right\}$ and $B = \left\{E^{F_1}; E^{F_2}; E^T\right\}$.

It can be shown, see [39] and [40] in the case of homogenizing 3D periodic material, that the problem to be solved can be written as follows:

$$[K] \left\{ \begin{array}{c} \{U\} \\ \left\{ \begin{array}{c} E^E \\ E^{F_1} \\ E^{F_2} \\ E^T \end{array} \right\} \end{array} \right\} = \left\{ \begin{array}{c} \{0\} \\ l \left\{ \begin{array}{c} N \\ M_1 \\ M_2 \\ M_3 \end{array} \right\} \end{array} \right\}, \tag{21}$$

where $[K]$ is the stiffness matrix. The loading is therefore imposed in the form of a given macroscopic strain, through the corresponding degrees of freedom. Computation of the right-hand side then provides the macroscopic axial force and moments. From (11), one can thus calculate the homogenised stiffness matrix $[a^{hom}]$.

As mentionned at the end of section 2, even if we have contact interaction, it is assumed that periodic boundary conditions can be applied. They are two set of boundary conditions, one for each components of the wire strand.

The solution to the problem (9) is defined up to a rigid body displacement, namely through three translations along the three main axes and a rotation around the main axis $\vec{y_3}$. It is necessary therefore to properly constrain this displacement to each strand component so as to obtain a unique solution. For this type of problem, the two possibilities consist of either using kinematic conditions [8] or solving the problem using an explicit integration scheme [9]. To simplify the generation of finite element models, an alternative method has been adopted here. Adding a viscous damping coefficient, as presented in [43], integrated into the classical Newton-Raphson scheme enables dissipating rigid body displacements. This viscous damping coefficient is evaluated throughout the simulation in order to guarantee a ratio of damping energy to total energy of less than 5 %, thus ensuring a negligible influence on the final solution.

4. Single-layer strand validation

A single-layer strand analysis, focusing on 6 helical wires and a central core,will first be presented to validate the models with solid and beam elements in a simple case. This configuration has been the subject of numerous studies based on analytical models [1], [4], [5] and numerical results [8], [9]. The various analyses pertain to the strand in tension, bending and torsion, as well as in a combined tension-bending state to highlight the nonlinear nature of the contact. The validation is based on the property that the solution of the microscopic problems provides, with the exception of edge effects, the stress state that would be obtained on a global structure subjected to a uniform strain state. Therefore, thanks to the periodic boundary conditions, it is not necessary to perform this global analysis on a large length of cable, but only to consider an axial period. One can then compare the solution of the microscopic problems with analytical solutions that are valid for a uniform strain state. This comparison will be made on the contact forces and stress fields.

4.1. Case study

The strand considered here is single-layer and composed of 7 steel wires. The geometric and material properties considered are listed in Table 1. To apply the periodic boundary conditions, model length is $l = 38.35$ mm, which corresponds to 1/6 of the layer pitch.

Table 1: Geometric and material properties of the single-layer strand

R_s [mm]	R_c [mm]	α [deg]	E[GPa]	ν
2.590	2.675	8.18	210	0.3

According to [4], lateral contact is neglected within the outer wire layer when two geometric conditions are met, namely:

$$\begin{cases} \xi_0 = \dfrac{R_s}{R_c} < 1 \\ \alpha < \alpha_{max} = arcos\left(\sqrt{\dfrac{tan^2(\pi/2 - \pi/n)}{(1+\xi_0^{-1})^2 - 1}}\right) \end{cases}, \tag{22}$$

where ξ_0 is the ratio between the wire radius of the outer layer and the core radius, and α_{max} is the maximum angle defining the beginning of lateral contact within the outer layer. In the present case, the conditions (22) are verified ($\xi_0 = 0.97$ and $\alpha_{max} = 11.86$ °), hence a purely radial contact within the strand can be assumed. The contact surface between the outer layer and the core reduces to a contact line. A friction coefficient $\mu = 0.3$ is set for tangential contact interactions.

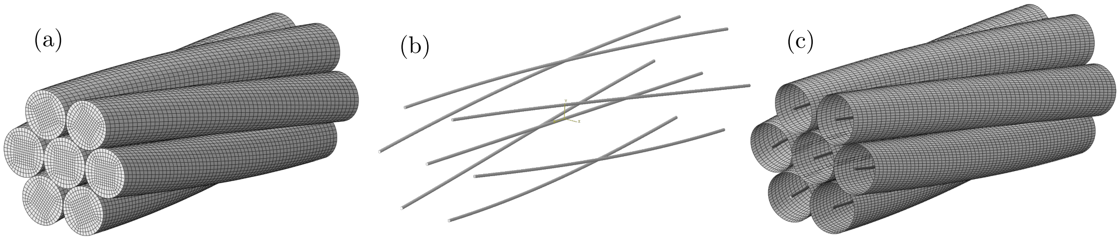

Figure 9: Display of the various meshes of the strand: (a) solid element model composed of 102,907 nodes and 92,400 C3D8 elements, (b) beam element model with 427 nodes and 420 B31 elements, and (c) beams with a surface element model containing 26,047 nodes, 420 B31 and 25,200 SFM3D4 elements

The various meshes are displayed in Figure 9. According to [9], mesh size may influence both global and local quantities such as strand stiffness, contact distribution and contact pressure between layers. Here, the element size has been chosen thanks a convergence study of two quantities of interest: the global homogenised stiffness and the contact normal transmission through its line load distribution over the core layer interface. The latter is computed for a tensile test. Three mesh densities: coarse, medium and fine have been considered and the medium one was found to provide the best compromise between accuracy and computation time.

By taking into account the rigid body constraints connecting the beam elements to the surface elements displayed in Figure 9.c, the number of independent degrees of freedom on the surface beam model is equal to that of the beam model with beam-to-beam contact.

4.2. Single-layer strand under a tensile load

An initial validation proposed consists of studying the strand under a tensile strain. For this purpose, an elongation of 0.1 % is applied to the strand. Figure 10a shows the strand's linear behaviour in tension. The stiffness results of the proposed models are compared with those of the theory developed by [1] and [4] with a relative difference of less than 2 %. The helical geometry of the outer layer implies a tension-torsion coupling, see Figure 10b. A comparison with results from the analytical models detailed in [3] and [4] shows a small relative difference of less than 2 %. Numerical models composed of beam elements seem to be slightly stiffer than the numerical model composed of solid elements.

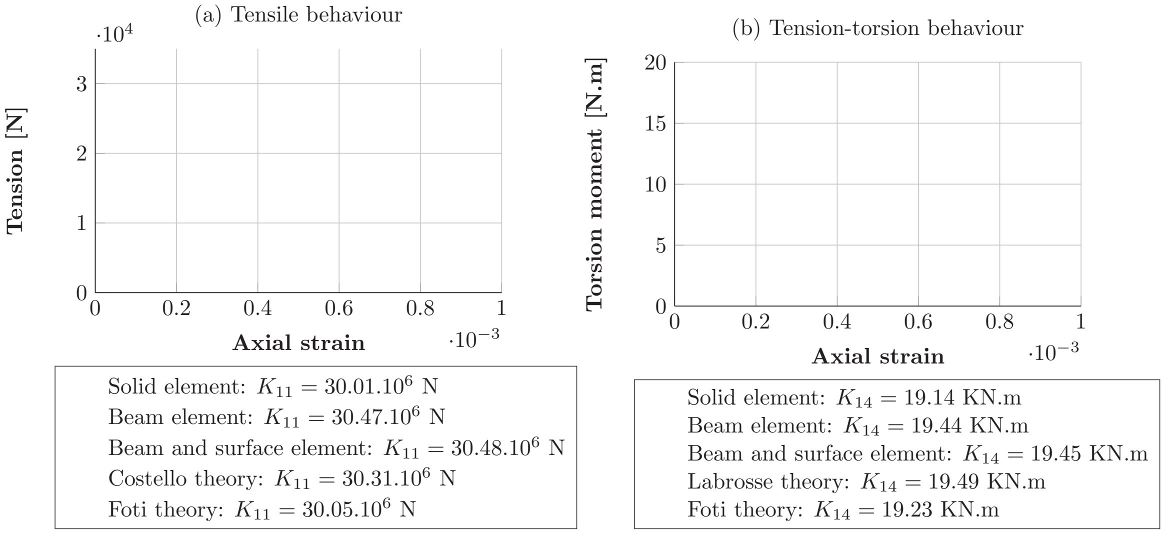

Figure 10: Single-layer strand behaviour under a tensile strain

The small difference in stiffness observed between numerical and analytical results can be explained by the contact problem solution. The influence of the friction coefficient during a tensile loading is negligible because small or no slip is present between strand components [44]. Only normal contact plays an important role in the tensile case. Contact forces summed over the contact line between the core and a layer wire are in good agreement with the theory developed in [5] and [14], with a relative difference of less than 2 %, see Figure 11a. This comparison validates application of the penalty method to solve normal contact problems for models with solid and beam elements. Use of the augmented Lagrangian method, coupled with the penalty method, also yields good results for the model featuring a beam with surface elements. The line load distribution in the normal direction is represented in Figure 11b. The contact surface discretisation with solid elements involves a periodic distribution of the contact forces. In the presence of a node-to-node contact, the contact force is indeed maximised, whereas when a node comes into contact with a surface, the contact force is minimised. Hence, the overall strand stiffness is reduced due to this variation along the contact line. A finer discretisation is necessary to approximate a contact line, therefore increasing the computation time [9]. The contact lineload distribution is better approximated with beam element models.

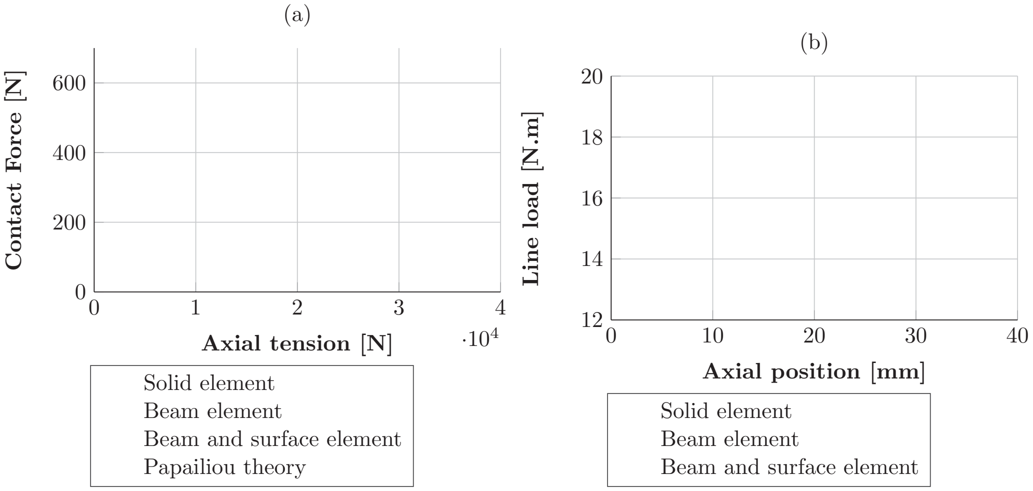

Figure 11: (a) Evolution in contact forces summed over the strand length between the core and a layer wire vs. axial tension, and (b) line load distribution between the core and a layer wire

The axial stress field, obtained in the central section of each numerical model, is displayed in Figure 12. As observed for the model with solid elements, axial stress concentrations result from contact. For models with beam elements, this phenomenon has not been captured since the axial stress is determined at each integration node of the section from beam theory. The maximum axial stress occurs at the central core, while the minimum stress is located on the outer layer wires. These wires work in bending, which therefore reduces their contribution to axial stiffness. Table 2 shows good agreement between the numerical models and Costello's analytical model. Costello's model is based on curved beams and is thus closer to the beam finite element model than to the solid element model.

Table 2: Layer wire axial stress of a single-layer strand subjected to a tensile strain: $E^E = 0.001$.

Model	$\sigma_{33} max$ [MPa]	$\sigma_{33} min$ [MPa]
Solid	204.9	185.0
Beam	207.8	203.7
Beam with surface	207.7	203.7
Costello	207.1	197.2

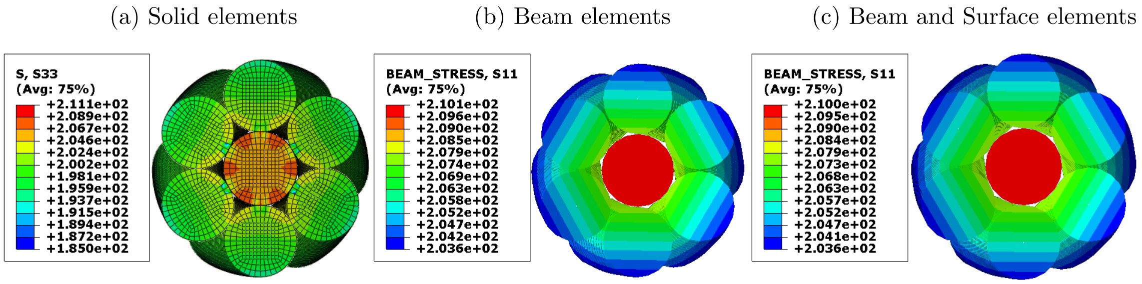
(a) Solid elements

(b) Beam elements

(c) Beam and Surface elements

Figure 12: Axial stress field σ_{33} at $y_3 = 0$ for the single-layer strand subjected to a tensile strain: $E^E = 0.001$

4.3. Single-layer strand under a torsional load

A torsion angle of 0.1 rad.m^{-1} is now imposed through the periodic boundary conditions. Figure 13 shows the linear behaviour in strand torsion. The numerical models are slightly stiffer in torsion than the models proposed by [1] and [4], with a relative difference of less than 4 %. A verification conducted on the torsion-tension coupling indicates that numerical results restore the stiffness matrix symmetry, i.e. $K_{14} = K_{41}$.

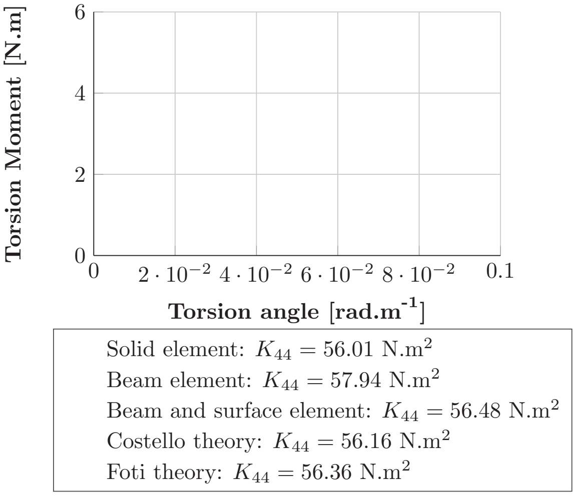

Figure 13: Single-layer strand behaviour under a torsional load

Figure 14 depicts the axial stress field obtained on the central section for a torsional strain. Due to the helical geometry of the outer layer, the wires are subjected to tension, bending and torsion. The maximum axial stress occurs in the outer fibre of each wire in the radial direction. The axial stress in the core equals zero since the core is not subjected to any elongation. In this configuration, the contact pressure exerted by the outer layer on the core is negligible. The maximum and minimum stress values are listed in Table 3. The lower stress values for the model with solid elements result from a more flexible torsion-tension behaviour. As regards the models with beam elements, numerical models tend to approximate the analytical model of [1] by relying on curved beams. The shear stresses for the central section are shown in Figure 15. The maximum and minimum shear stress values are located on the central core, which has the largest radius. A comparison of the maximum and minimum values of the numerical models and Costello's theory is drawn in Table 4, which reveals a good level of agreement.

Table 3: Layer wire axial stress of a single-layer strand subjected to a torsional strain: $E^T = 0.1$ rad.m^{-1}

Model	$\sigma_{33}max$ [MPa]	$\sigma_{33}min$ [MPa]
Solid	23.47	5.40
Beam	30.48	0.60
Beam and surface	30.38	0.01
Costello	30.20	0.00

Table 4: Layer wire shear stress of a single-layer strand subjected to a torsional strain: $E^T = 0.1$ rad.m^{-1}

Model	$\sigma_{13}max$ [MPa]	$\sigma_{13}min$ [MPa]
Solid	23.58	-23.58
Beam	20.10	-20.10
Beam and surface	20.16	-20.16
Costello	20.28	-20.28

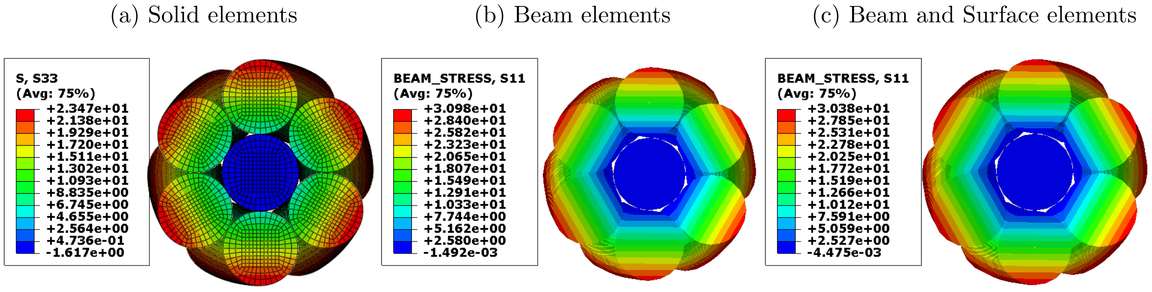
(a) Solid elements

(b) Beam elements

(c) Beam and Surface elements

Figure 14: Axial stress field σ_{33} at $y_3 = 0$ for the single-layer strand subjected to a torsional strain: $E^T = 0.1$ rad.m^{-1}.

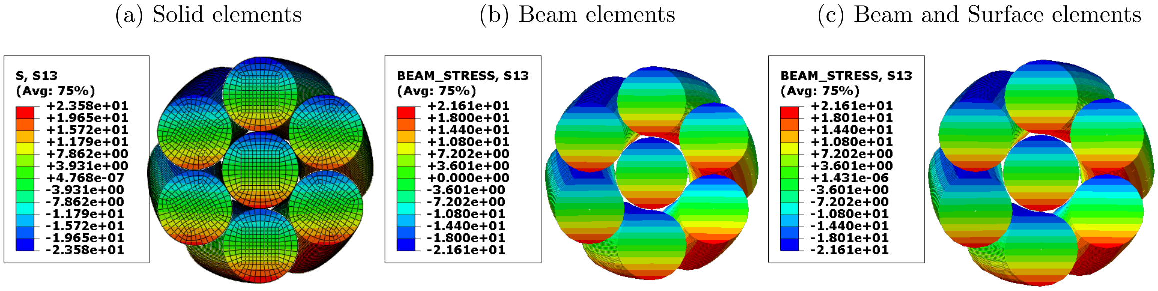
(a) Solid elements

(b) Beam elements

(c) Beam and Surface elements

Figure 15: Shear stress field σ_{13} at $y_3 = 0$ for the single-layer strand subjected to a torsional strain: $E^T = 0.1$ rad.m^{-1}.

4.4. Single-layer strand under a bending load

Let's now consider a pure bending load. A curvature of 0.1 m^{-1} is applied to the strand around the $\vec{y_1}$-axis. The behaviour obtained for the numerical models is compared with Papailiou's theory, see Figure 16, with a relative difference of less than 0.5 %. In the case of pure bending, normal contact stresses are negligible, and each layer wire is free to slip [8]. Due to the very low frictional stresses, the influence of the friction coefficient is also negligible. Strand behaviour in pure bending is therefore linear and bending stiffness is minimal. Figure 17 shows that the longitudinal sliding of layer wires is in good agreement with the equation of a loxodromic curve, see Eq.(5).

The axial stress field, see Figure 18, indicates that each wire is in pure bending. As demonstrated in [8], when the cable is subjected to pure bending, all the wires are also subjected to pure bending. Maximum stress occurs in the core by virtue of having the largest radius. The maximum and minimum stresses in a layer wire are listed in Table 5. Once again, the numerical values are very similar to those from the theory proposed by Papailiou [5].

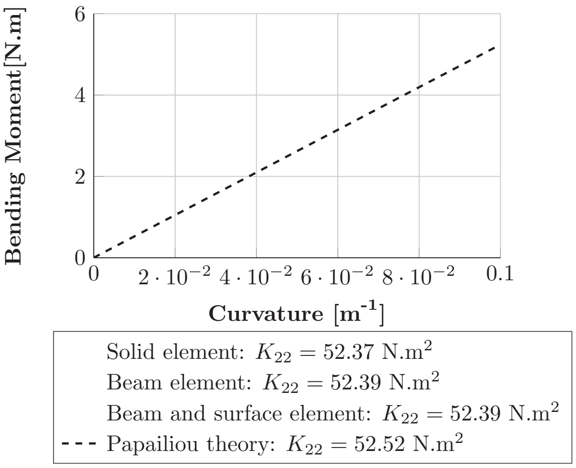

Figure 16: Single-layer strand behaviour in bending subjected to a curvature $E^{F_1} = 0.1$ m^{-1}

Table 5: Layer wire axial stress of a single-layer strand subjected to pure bending: $E^{F_1} = 0.1$ m^{-1}

Model	$\sigma_{33}max$ [MPa]	$\sigma_{33}min$ [MPa]
Solid	51.97	-51.97
Beam	53.71	-53.70
Beam with surface	53.69	-53.11
Papailiou	53.84	-53.84

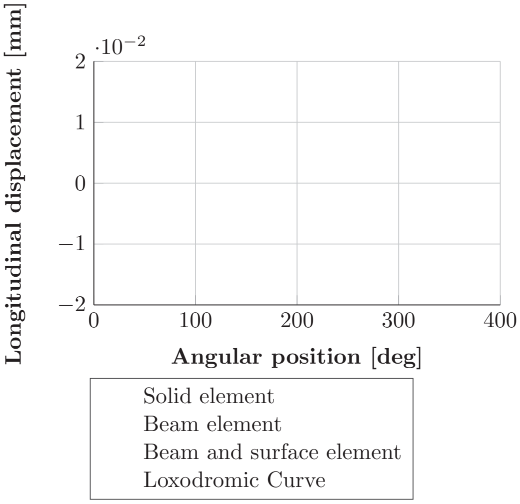

Figure 17: Longitudinal slip along $\vec{y_3}$ of a layer wire for a curvature $E^{F_1} = 0.1$ m^{-1}.

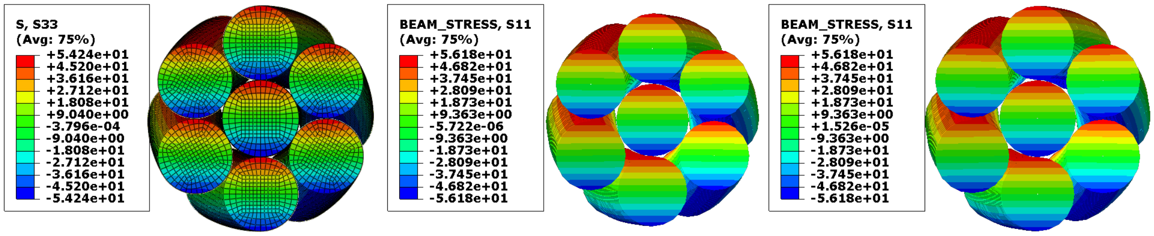
(a) Solid elements

(b) Beam elements

(c) Beam and Surface elements

Figure 18: Axial stress field σ_{33} at $y_3 = 0$ for the single-layer strand subjected to pure bending: $E^{F_1} = 0.1$ m^{-1}

4.5. Single-layer strand under a bending load with an initial tensile load

To highlight contact nonlinearity, a study of the strand subjected to a tension-bending loading will now be presented. The strand is initially loaded in tension by an elongation of 0.1%, then a curvature of 0.1 m^{-1} is applied around the $\vec{y_1}$-axis.

The overall behaviour obtained for each numerical model is presented in Figure 19. This behaviour can be separated into several regions, depending on curvature intensity. Initially, the bending stiffness is maximised because all strand components are maintained by the normal contact forces produced by tensile loading. In this case, the layer wires and core behave as a single solid, and the cross-section undergoes overall bending, see Figure 20. The bending stiffnesses obtained by numerical models in the stick state are lower than the bending stiffness computed by analytical models, see Table 6. This finding is explained by the fact that analytical models are based on a perfect geometry and assumed to contain perfectly bonded components at the initial state, in excluding any sliding. On the other hand, small slips are always present in numerical models that tend to decrease strand stiffness in the stick state. To more closely approximate analytical models, it would be necessary to refine the mesh of the contact areas, see [9], which would greatly increase computation time, especially for solid elements. One can also check that the discrepancy between solid element model and analytical solution reported in Table 6 is close to that obtained in [9]. From a critical curvature, i.e. around 0.015 m^{-1}, layer wires close to the bending axis start to slip. Each wire then undergoes pure bending, and bending stiffness decreases to its minimum value, which corresponds to that obtained in the previous section, see Figure 21.

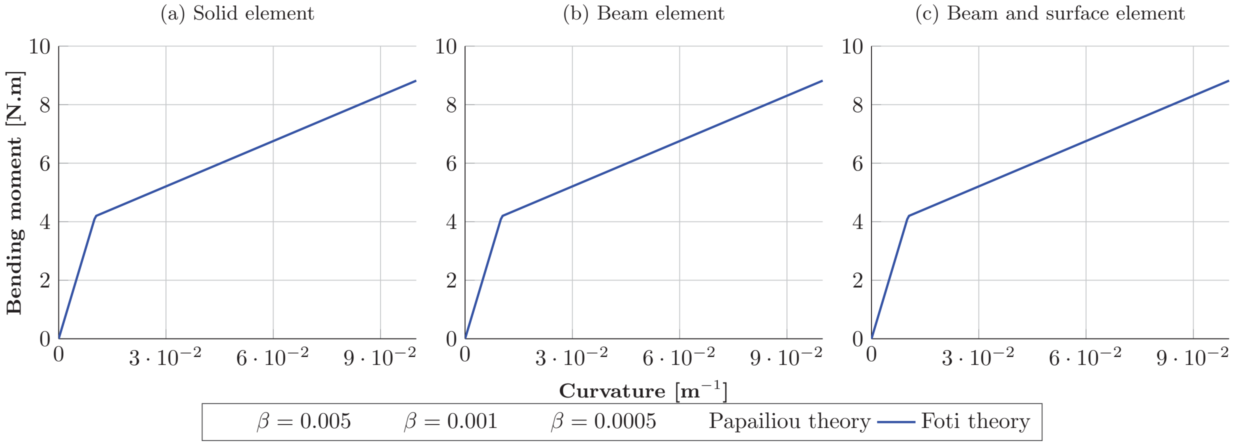

Figure 19: Single-layer strand behaviour in bending with an initial tensile load for several values of β.

Table 6: Single-layer strand bending stiffness under bending with an initial tensile load for both the stick and slip states, with $\beta = 0.0005$.

Model	K_{22} stick state [N.m^2]	K_{22} slip state [N.m^2]
Solid	320.55	52.30
Beam	411.00	51.83
Beam and surface	378.58	52.99
Papailiou	409.43	52.52
Foti	408.54	51.63

A strong influence from the numerical coefficient β on numerical behaviour is obtained. With the default value of β given in ABAQUS, i.e. $\beta = 0.005$, stick state behaviour is poorly reproduced. It is therefore necessary to define the lowest possible coefficient β to approximate Coulomb's Law while ensuring solution convergence. In the present case, convergence of the moment-curvature curve is obtained for $\beta = 0.0005$.

For the stick behaviour, the axial stress distribution is shown in Figure 20. As explained previously for the beam model, axial stress varies linearly across the cross-section, while for a model with solid elements, the effect of contact forces can be observed. Stress values in the outer layer of the numerical models are listed in Table 7 and compared with Papailiou's theoretical output in the stick state. Given that some slip occurs in the numerical models, the maximum stress values are slightly lower than those of the analytical model.

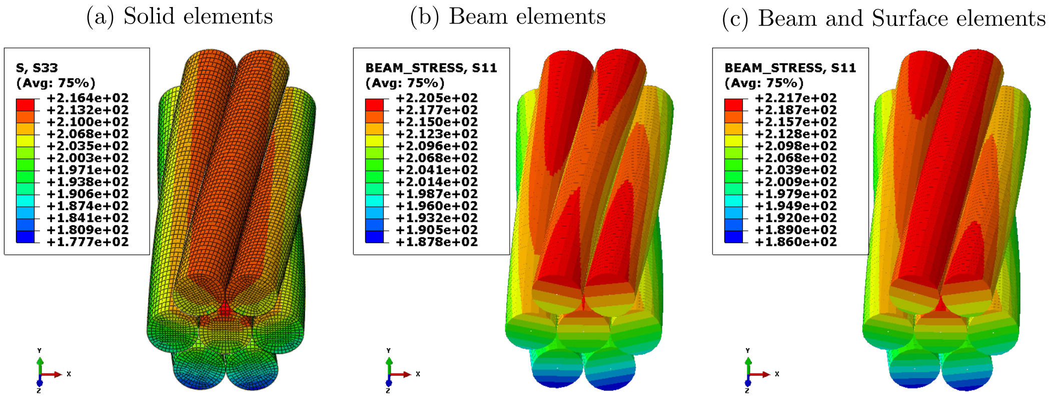
(a) Solid elements (b) Beam elements (c) Beam and Surface elements

Figure 20: Axial stress field σ_{33} for the single-layer strand under bending with initial tensile load: $E^E = 0.001$ and $E^{F_1} = 0.00875$ m^{-1}, in the stick state

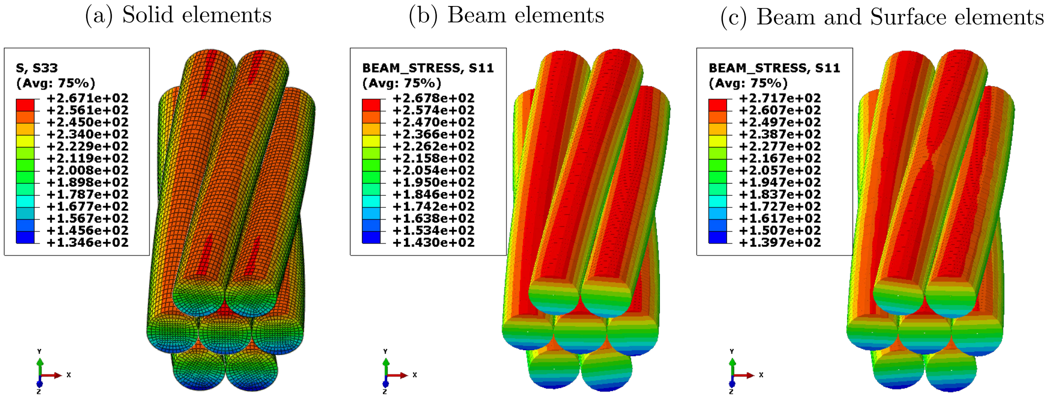
(a) Solid elements (b) Beam elements (c) Beam and Surface elements

Figure 21: Axial stress field σ_{33} for the single-layer strand under bending with an initial tensile load: $E^E = 0.001$ and $E^{F_1} = 0.1$ m^{-1}, in the slip state

For sliding behaviour, as observed in Figure 21, each wire undergoes pure bending. The maximum stress is located on the strand core due to its larger radius. The numerical values are listed in Table 8 and compared to the analytical results stemming from Papailiou's theory, in showing a good level of agreement.

The computational efficiency of each numerical model is presented in Table 9. For the single-layer strand, the beam model significantly reduces model size and computation time by a factor of 30, in comparison with the solid element model. Beam elements associated with surface elements slightly improve contact modelling and reduce computation time by a factor of 16, in comparison with the solid element mesh. The beam-to-beam contact solution seems to be more efficient than a beam with surface elements in solving the line contact problem.

Table 7: Layer wire axial stress of a single-layer strand under bending with an initial tensile load: $E^E = 0.001$ and $E^{F_1} = 0.00875$ m^{-1} in the stick state

Model	$\sigma_{33}max$ [MPa]	$\sigma_{33}min$ [MPa]
Solid	213.1	177.7
Beam	220.4	187.8
Beam and surface	221.7	186.0
Papailiou	221.4	192.7

Table 8: Layer wire axial stress of a single-layer strand under bending with an initial tensile load: $E^E = 0.001$ and $E^{F_1} = 0.1$ m^{-1} in the slip state

Model	$\sigma_{33}max$ [MPa]	$\sigma_{33}min$ [MPa]
Solid	257.3	134.6
Beam	267.8	143.0
Beam and surface	268.2	139.7
Papailiou	276.1	139.6

Table 9: Computation time comparison between finite element models for a tensile and bending loading (i7-6700HQ CPU 2,60 GHz with 8 Go Ram)

Model	CPU time [s]
Solid	1395
Beam	46.4
Beam with surface	89

5. Multi-layer strand validation

Let's now consider a simple multi-layer strand, composed of 2 helical wire layers and a cylindrical circular core. Two contact types are present, in the form of a contact line between the core and the first layer, while contact points are also present between the first and second layers. The axial strand behaviour is analysed through a tensile loading, and contact nonlinearities will be highlighted through a loading in both tension and bending.

5.1. Case study

The strand currently studied is composed of 19 steel wires, including 12 on the outer layer, 6 on the inner layer and one central wire for the core. The geometry used and material properties are presented in Table 10.

Table 10: Geometric and material properties of the multi-layer strand

Layer	R[mm]	α[deg]	E[GPa]	ν
Core	2.675	-	210	0.3
1	2.590	-8.24	210	0.3
2	2.590	8.18	210	0.3

The multi-layer strand chosen here satisfies the two geometric conditions, see Eq. (22), making it possible to neglect the lateral contact between wires of the same layer, i.e.:

- For the inner layer: $\xi_0 = 0.97 < 1$ and $\alpha_{max} = 11.86°$.
- For the outer layer: $\xi_0 = 0.33 < 1$ and $\alpha < \alpha_{max} = 17.20°$.

Therefore, only the radial contact between the core and the inner layer and between the inner layer and the outer layer is taken into account. The former is established along a contact line while the latter is a series of contact points. A friction coefficient $\mu = 0.3$ is chosen for all contact interactions.

The various meshes are shown in Figure 22. Using the same wire geometric properties than the single layer strand, 60-element axial discretisation is selected for each model presented here. By taking into account the rigid body equations connecting beam elements to surface elements, the number of independent degrees of freedom for both beam models is the same.

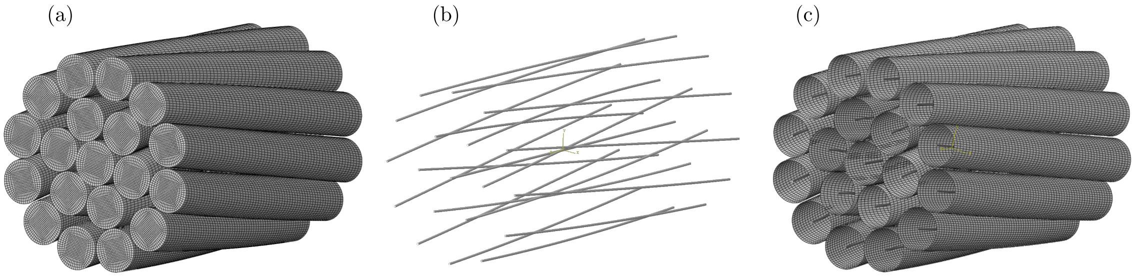

Figure 22: Display of the various meshes of the multi-layer strand: (a) solid element model composed of 520,391 nodes and 478,800 C3D8 elements, (b) beam element model with 1,159 nodes and 1,140 B31 elements, and (c) beams with surface elements model containing 70,699 nodes, and 1,140 B31 and 68,400 SFM3D4 elements

5.2. Multi-layer strand under a tensile load

For the first analysis, an axial deformation of 0.1% is applied to the strand. A comparison of numerical simulations with analytical models from [1] and [4] reveals a very good level of agreement, see Table 11. It can be noticed that despite opposite lay angles for the inner and outer layers, the larger number of wires in the outer layer produces a tension-torsion coupling.

Table 11: Tension and tension-torsion stiffness from the multi-layer strand at $E^E = 0.001$

Model	K_{11} [10^7 N]	K_{14} [KN.m]
Solid	7.97	56.25
Beam	8.11	56.97
Beam and surface	8.12	57.05
Costello	8.16	57.71

For a tensile strain, only normal contact influences strand behaviour. As for the single-layer strand, see 11a, a very good level of agreement has been obtained with Papailiou's model for contact forces. The contact pressure generated by the outer layer on the inner layer greatly influences contact pressure between the latter and the core. However, the line load distribution differs from one model to another, see Figures 23 and 24. The contact force distribution between the core and the inner layer depends on the contact points between the inner and outer layers. For models with beam elements, the maximum values of normal contact forces between the core and inner layer are in good agreement with the axial contact positions between the inner and outer layers. For the model with solid elements, this observation is less obvious. As in the case of the single-layer strand, the contact resolution for a model with solid elements will strongly depend on the mesh. Therefore, one of the advantages of 3D models, i.e. the ability to take contact forces into account for stress computations, is offset by the requirement of a very fine mesh for obtaining accurate stresses in the vicinity of contact zones.

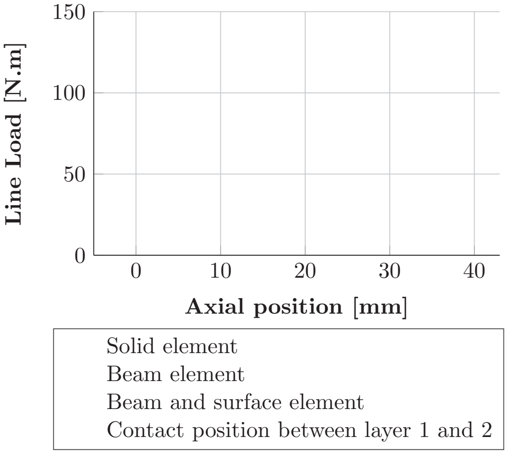

Figure 23: Line load distribution between the inner layer wire and the core

The axial stress field for a tensile loading is shown in Figure 24 for the inner layer and in Figure 25 for the outer layer. Each model reveals the impact of a contact point on the axial stress distribution within the outer layer. When the outer layer wire is not in contact with an inner layer wire, the wire section works in bending, with a maximum stress at the lower fibre of the wire in the radial direction. Conversely, when the outer layer wire is in contact with an inner layer wire, the wire is still subjected to a bending moment, such that the maximum stress lies on the upper fibre of the wire in the radial direction. Therefore, the outer layer wire section undergoes local bending with a moment whose sign changes as a function of the contact position between the two layers.

The minimum and maximum axial stress values are listed in Table 12. In the outer layer, the maximum stress values obtained from numerical models are consistent with one another. Significant differences appear between solid element and beam element results with respect to minimum stress values. These differences can also be seen for the minimum and maximum stresses in the inner layer. In this inner layer, the stress distribution is similar to that observed for the single-layer strand, with higher stress variations in the contact areas between the outer and inner layers. For the maximum stress value in the outer layer, numerical results from the various models are again consistent. The minimum stress value in the outer layer differs between the solid element models and beam element models. As noted earlier, this difference stems mainly from the capability of the solid element model to account for the local stress concentrations due to contact. Compressive stresses can also be locally observed in elements making contact with the inner layer in the solid element model.

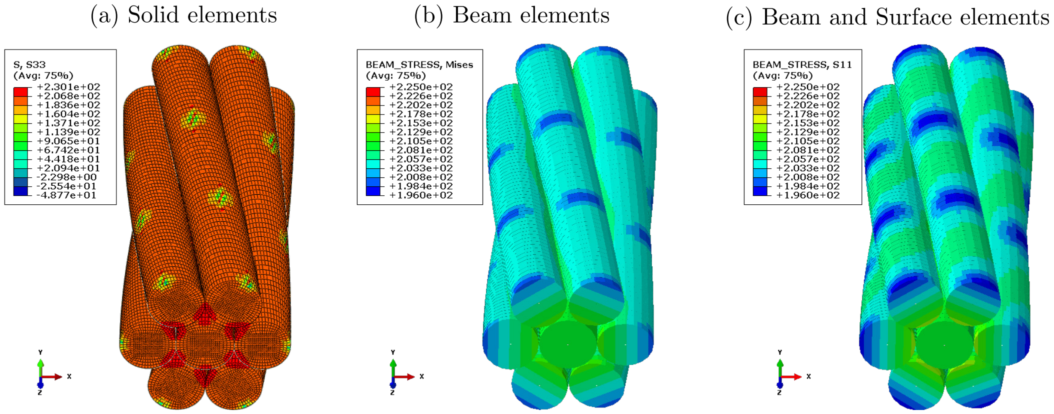
(a) Solid elements

(b) Beam elements

(c) Beam and Surface elements

Figure 24: Axial stress field σ_{33} in the inner layer and the core for the multi-layer strand under a tensile load: $E^E = 0.001$, thus highlighting contact position between the inner and outer layers

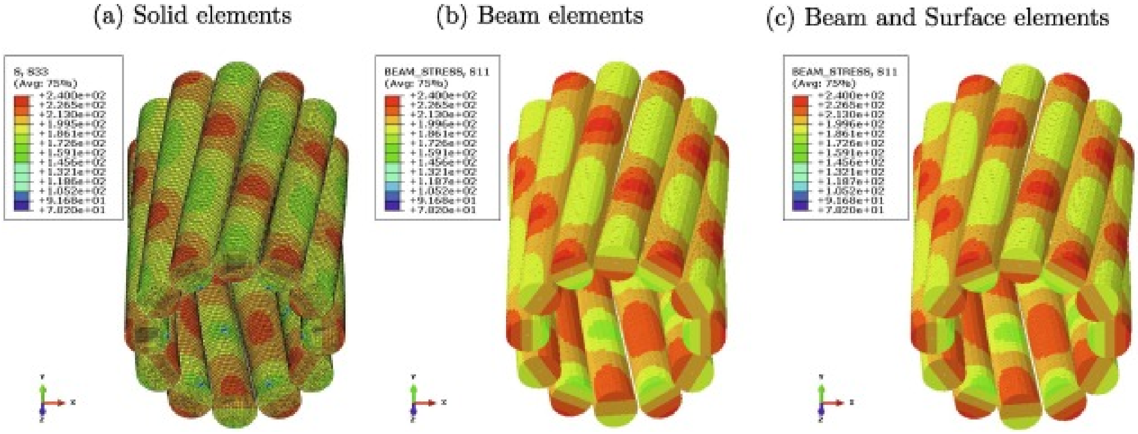
(a) Solid elements

(b) Beam elements

(c) Beam and Surface elements

Figure 25: Axial stress field σ_{33} in the outer layer for the multi-layer strand under a tensile load: $E^E = 0.001$

Axial stress values given by Costello's model are given in Table 12 for information purposes. Although the beam model results lie close to Costello's theory for the inner layer, a departure can be noticed in the outer layer; this discrepancy originates from contact points, which are not taken into account in Costello's model.

Table 12: Layer wire axial stress of a multi-layer strand subjected to a tensile strain: $E^E = 0.001$. (*) Contact line assumption between inner and outer layer.

Model	Outer layer		Inner layer	
	σ_{33}max [MPa]	σ_{33}min [MPa]	σ_{33}max [MPa]	σ_{33}min [MPa]
Solid	233.0	78.2	230.1	-48.8
Beam	234.5	175.3	211.5	199.8
Beam and surface	232.9	177.6	214.0	197.2
Costello*	205.1	201.0	207.1	197.6

5.3. Multi-layer strand under a bending load with an initial tensile load

The strand is now subjected to both a tensile and bending strain. The contacts are initialised by an axial strain of 0.1%; next, a curvature of 0.1 m^{-1} is applied to the structure around the $\vec{y_1}$-axis.

The bending behaviour is presented in Figure 26. Three phases can be identified: first the stick state, then slipping of the outer layer, and lastly slipping of the inner layer. According to Papailiou's theory [5], the critical curvature of sliding is defined by a mean critical curvature for each wire layer. The analytical bending moment is therefore piecewise linear. For numerical models, wire sliding is evaluated throughout the simulation, which leads to smoothing the behaviour.

The influence of coefficient β can once again be noticed. For low values of β, numerical behaviour tends to be stiffer in the stick state, approaching the maximum stiffness estimated by Papailiou's theory, see Table 13. These results converge when β reaches a value of 0.0005. The various contact models also influence bending behaviour. The results obtained from both the beam-to-beam contact model and the beam with surface elements model lie close to the analytical values. As in the case of the single-layer strand, the discrepancy between solid element model and analytical solution is large. However, the numerical models are in good agreement with the bending stiffness in the total sliding state, see Table 13.

A cyclic loading in bending, with an amplitude of 0.2 m^{-1}, is proposed in Figure 27, thereby highlighting the hysteresis cycle of the strand. The difference between analytical and numerical results tends to increase during both the discharge and second charge phases. A good level of agreement can be observed between the finite element results and the analytical model.

Table 13: Multi-layer strand bending stiffness under bending with an initial tensile load for the stick and slip state with $\beta = 0.0005$.

Model	K_{22} stick state [N.m^2]	K_{22} slip state [N.m^2]
Solid	1738.4	139.5
Beam	3366.7	148.9
Beam and surface	2912.9	140.3
Papailiou	3306.8	140.8

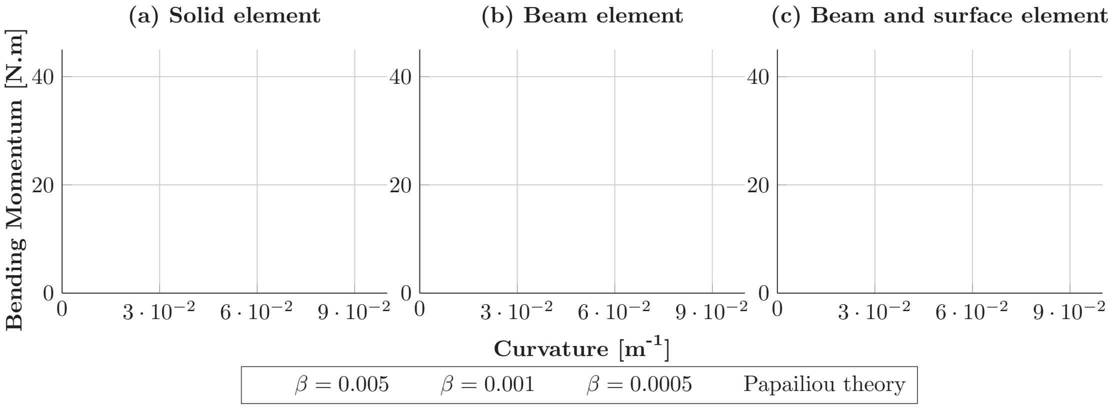

Figure 26: Multi-layer strand behaviour in bending with an initial tensile load for several values of β.

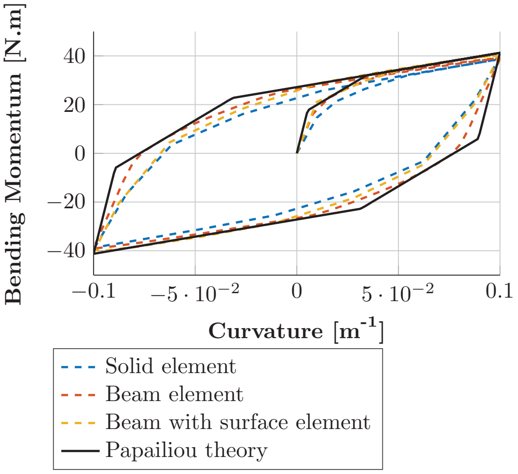

Figure 27: Hysteresis strand behaviour with a curvature amplitude of 0.2 m^{-1}: Comparison between the numerical model with $\beta = 0.005$ and Papailiou's theory

Figure 29 shows the axial stress field in the various layers for a sliding behaviour. As in the case of the single-layer strand, it can be remarked that all strand wires are subjected to pure bending. The variation between maximum and minimum stresses therefore increases with a sliding behaviour, see Table 15. The two beam element models output the same results. As opposed to beam element models, the axial stresses with the solid element model are locally greater for a contact position in the inner layer.

The axial stress values obtained by Papailiou's theory are given for information in Tables 14 and 15. The beam models agree with the theory for stresses within the inner layer. However, Papailiou's theory, which does not consider contact points, does underestimate the axial stresses in the outer layer.

As indicated in Table 16, the computation time associated with beam models is very low compared to that of solid element models. In comparison with the beam-to-beam contact model, use of the beam with surface elements model reduces computation time by a factor of 5 and seems to be more efficient in solving the contact point problem.

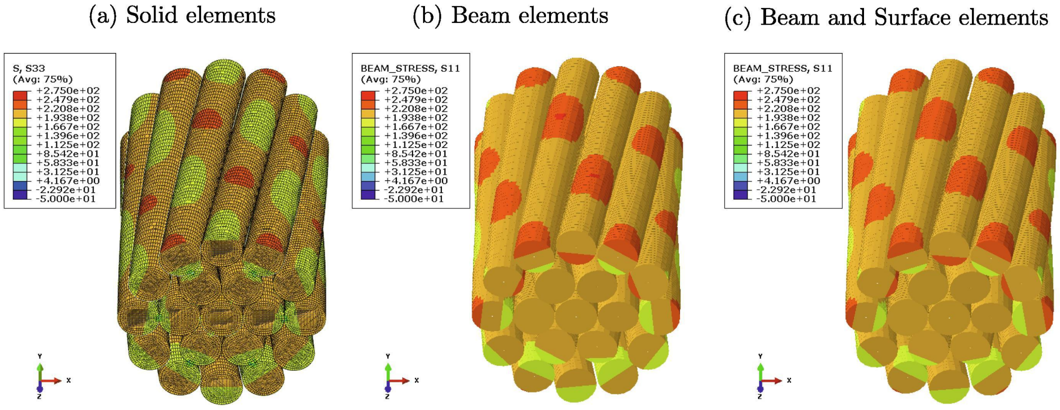
(a) Solid elements (b) Beam elements (c) Beam and Surface elements

Figure 28: Axial stress field σ_{33} for the multi-layer strand under bending with an initial tensile load: $E^E = 0.001$ and $E^{F_1} = 0.005$ m^{-1}, in the stick state

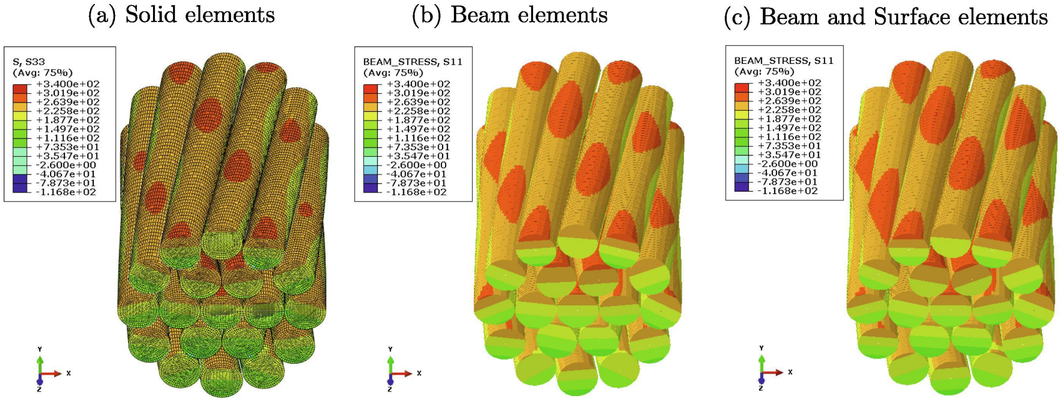
(a) Solid elements (b) Beam elements (c) Beam and Surface elements

Figure 29: Axial stress field σ_{33} for the multi-layer strand under bending with an initial tensile load: $E^E = 0.001$ and $E^{F_1} = 0.1$ m^{-1}, in the stick state

Table 14: Layer wire axial stress of a multi-layer strand under bending with an initial tensile load: $E^E = 0.001$ and $E^{F_1} = 0.005$ m^{-1}, in the stick state (*) Contact line assumption between inner and outer layers.

Model	Outer layer		Inner layer	
	σ_{33}max [MPa]	σ_{33}min [MPa]	σ_{33}max [MPa]	σ_{33}min [MPa]
Solid	258.8	67.0	247.5	-48.9
Beam	248.6	169.7	214.7	201.8
Beam and surface	243.7	172.7	213.8	201.2
Papailiou*	221.2	194.5	215.9	199.8

Table 15: Layer wire axial stress of a multi-layer strand under bending with an initial tensile load: $E^E = 0.001$ and $E^{F_1} = 0.1$ m^{-1}, in the slip state (*) Contact line assumption between inner and outer layers.

Model	Outer layer		Inner layer	
	σ_{33}max [MPa]	σ_{33}min [MPa]	σ_{33}max [MPa]	σ_{33}min [MPa]
Solid	318.9	-71.3	338.0	-116.8
Beam	299.4	166.2	283.6	122.3
Beam and surface	300.9	162.6	287.0	112.3
Papailiou*	276.1	139.6	290.9	125.2

Table 16: Computation time comparison between finite element models for a tensile and bending load (8-core Intel Xeon (Haswell) E5-2680v3 CPUs 2.50GHz with 128 Go Ram)

Model	CPU time [min]
Solid	367
Beam	38
Beam and surface	7

6. Conclusion

This paper has proposed a new computational approach for studying the overall behaviour and local stress state of strand-type structures. This method is based on the homogenization theory of periodic structures, with the local problem posed on the strand axial period being solved using the finite element method. This approach fully utilises the strand's helical symmetry, thus minimising the size of the computational domain. Consequently, accounting for geometric complexity and contact interactions, which are of paramount importance for bending loads, is more straightforward. The size of the numerical model can also be reduced thanks to the use of beam elements, and one objective of this paper has been to assess the accuracy of such a model, in comparison with solid element models and analytical results.

An initial validation case study was performed on a single-layer strand; it was shown that for each loading case, the various numerical models, with both solid elements and beam elements, reproduced the single-layer strand behaviour in close agreement with several analytical models. The three numerical models all led to very similar results. The differences stem mainly from the contact model, which differs from one model to another. For a model with solid elements, a finer mesh becomes necessary in the vicinity of contact zones in order to obtain accurate stresses. This configuration increases computation time, especially with sections containing a large number of wires. Beam models provide a very good compromise between accuracy and numerical efficiency. In addition, the use of a contact surface associated with the beam elements appears to be more efficient than beam-to-beam contact. This formulation facilitates contact detection and improves solution convergence even in the case of large sliding. Nevertheless, beam modelling does not allow taking local contact forces into account during stress computations.

For the second example, a multi-layer strand was studied to show the influence of a second layer of wires on strand behaviour. In addition to the contact line between the core and the inner layer, a contact point distribution exists between the inner and outer layers. It has also been demonstrated that the overall behaviour in tension and tension-bending obtained by the analytical model can be reproduced by each numerical model. In contrast, regarding local axial stresses, a discrepancy was found between numerical and analytical results; the numerical models indeed suggest a significant influence of contact points between the inner and outer layers on the axial stress distribution. Stress concentrations occur at each contact location, thereby locally increasing the maximum stress value and decreasing the minimum stress value. In this case, analytical models prove to be inadequate since they fail to take contact points into account.

7. Acknowledgments

This work has received support from France Energies Marines, along with State subsidies managed by the National Research Agency, as part of the Investments for the Future program, under the reference ANR-10-IEED-0006-28.

References

[1] G. Costello, Theory of wire rope, Springer-Verlag, 2nd edition, 1997.

[2] S. Ghoreishi, Modélisation analytique et caractérisation expérimentale du comportement de câbles synthétiques, Ph.D. thesis, École Centrale de Nantes (France), 2005.

[3] M. Labrosse, Contribution à l'étude du rôle du frottement sur le comportement et la durée de vie des câbles monocouches., Ph.D. thesis, École Centrale de Nantes (France), 1998.

[4] F. Foti, L. Martinelli, Modeling the axial-torsional response of metallic strands accounting for the deformability of the internal contact surfaces: Derivation of the symmetric stiffness matrix, International Journal of Solids and Structures 171 (2019) 30–46.

[5] K. Papailiou, On the bending stiffness of transmission line conductors, IEEE Transactions on Power Delivery (1997) 1576–1588.

[6] F. Foti, L. Martinelli, An analytical approach to model the hysteretic bending behavior of spiral strands, Applied Mathematical Modelling 40 (2016) 6451–6467.

[7] F. Foti, A. de Luca di Roseto, Analytical and finite element modelling of the elastic–plastic behaviour of metallic strands under axial–torsional loads, International Journal of Mechanical Sciences 115-116 (2016) 202–214.

[8] W. Jiang, A concise finite element model for pure bending analysis of simple wire strand, International Journal of Mechanical Sciences 54 (2012) 69–73.

[9] D. Zhang, M. Ostoja-Starzewski, Finite Element Solutions to the Bending Stiffness of a Single-Layered Helically Wound Cable With Internal Friction, Journal of Applied Mechanics 83 (2016) 031003.

[10] Y. Yu, Z. Chen, H. Liu, X. Wang, Finite element study of behavior and interface force conditions of seven-wire strand under axial and lateral loading, Construction and Building Materials 66 (2014) 10–18.

[11] S. Kmet, E. Stanova, G. Fedorko, M. Fabian, J. Brodniansky, Experimental investigation and finite element analysis of a four-layered spiral strand bent over a curved support, Engineering Structures 57 (2013) 475–483.

[12] R. Judge, Z. Yang, S. Jones, G. Beattie, Full 3D finite element modelling of spiral strand cables, Construction and Building Materials 35 (2012) 452–459.

[13] J. Wu, The finite element modeling of spiral ropes, International Journal of Coal Science & Technology 1 (2014) 346–355.

[14] R. Baumann, P. Novak, Efficient computation and experimental validation of ACSR overhead line conductors under tension and bending, Cigre Science Engineering 9 (2017) 5–7.

[15] C. Yu, S. Yin, B. Dong, Y. Bao, The Analysis of 91-Wire Strand Tensile Behavior Using Beam Finite Element Model, IOP Conference Series: Materials Science and Engineering 381 (2018) 012115.

[16] F. Bussolati, M. Guiton, Y. Poirette, M. Martinez, P. Guidault, O. Allix, A new fully-detailled finite element model of spiral strand wire ropes for fatigue life estimate of a mooring line, International Conference on Ocean, Offshore and Arctic Engineering 38 (2019) 10.

[17] I. Páczelt, R. Beleznai, Nonlinear contact-theory for analysis of wire rope strand using high-order approximation in the FEM, Computers & Structures 89 (2011) 1004–1025.

[18] S. Lalonde, R. Guilbault, F. Légeron, Modeling multilayered wire strands, a strategy based on 3D finite element beam-to-beam contacts - Part I: Model formulation and validation, International Journal of Mechanical Sciences 126 (2017) 281–296.

[19] D. Durville, Contact-friction modeling within elastic beam assemblies: an application to knot tightening, Computational Mechanics 49 (2012) 687–707.

[20] P. D. T.D. Vu, D. Durville, Finite element simulation of the mechanical behavior of synthetic braided ropes and validation on a tensile test, International Journal of Solids and Structures 58 (2015) 106–116.

[21] G. Z. P. Wriggers, On contact between three-dimensional beams undergoing large deflections, Communications in Numerical Methods in Engineering 13 (1997) 429–438.

[22] A. Frikha, P. Cartraud, F. Treyssède, Mechanical modeling of helical structures accounting for translational invariance. Part 1: Static behavior, International Journal of Solids and Structures 50 (2013) 1373–1382.

[23] N. Karathanasopoulos, G. Kress, Two dimensional modeling of helical structures, an application to simple strands, Computers & Structures 174 (2016) 79–84.

[24] P. Cartraud, T. Messager, Computational homogenization of periodic beam-like structures, International Journal of Solids and Structures 43 (2006) 686–696.

[25] E. Stanova, G. Fedorko, M. Fabian, S. Kmet, Computer modelling of wire strands and ropes Part I: Theory and computer implementation, Advances in Engineering Software 42 (2011) 305–315.

[26] P. Wriggers, Computational Contact Mechanics, Springer, Berlin, Heidelberg, 2006.

[27] F. Foti, L. Martinelli, Mechanical modeling of metallic strands subjected to tension, torsion and bending, International Journal of Solids and Structures 91 (2016) 1–17.

[28] K. Feyrer, Wire Ropes: Tension, Endurance, Reliability., Springer, Berlin, Heidelberg, 2007.

[29] D. Boso, M. Lefik, B. Schrefler, A multilevel homogenised model for superconducting strand thermomechanics, Cryogenics 45 (2005) 259–271.

[30] B. S. M. Kamiński, Probabilistic effective characteristics of cables for superconducting coils, Computer Methods in Applied Mechanics and Engineering 188 (2000) 1–16.

[31] N. Buannic, P. Cartraud, Higher-order effective modeling of periodic heterogeneous beams. I. Asymptotic expansion method, International Journal of Solids and Structures (2001) 38:7139–7161.

[32] A. Kolpakov, Calculation of the characteristics of thin elastic rods with a periodic structure, Journal of Applied Mathematics and Mechanics 55 (1991) 358–365.

[33] J. Kim, M. Cho, E. Smith, An asymptotic analysis of composite beams with kinematically corrected end effects, International Journal of Solids and Structures 45 (2008) 1954–1977.

[34] R. B. W.C. Young, Roark's Formulas for Stress and Strain, McGraw-Hill, 7 edition, 2002.

[35] M. Smith, ABAQUS/Standard User's Manual, Version 6.14, Simulia, 2009.

[36] K. S. A. Konyukhov, Geometrical covariant approach for contact between curves representing beam and cable type structures, PAMM 8 (2008) 10299 – 10300.

[37] P. W. A. Gay Neto, P.M. Pimenta, Self-contact modeling on beams experiencing loop formation, Comput. Mech. 55 (2015) 193–208.

[38] F. Bussolati, Modèle multi-échelle de la fatigue des lignes d'ancrage câblées pour l'éolien offshore flottant, Ph.D. thesis, Université Paris-Saclay (France), 2019.

[39] J. Michel, H. Moulinec, P. Suquet, Effective properties of composite materials with periodic microstructure: a computational approach, Computer Methods in Applied Mechanics and Engineering 172 (1999) 109–143.

[40] H. Magoariec, S. Bourgeois, O. Débordes, Elastic plastic shakedown of 3D periodic heterogeneous media: a direct numerical approach, International Journal of Plasticity 20 (2004) 1655–1675.

[41] S. Yi, L. Xu, G. Cheng, Y. Cai, FEM formulation of homogenization method for effective properties of periodic heterogeneous beam and size effect of basic cell in thickness direction, Computers & Structures 156 (2015) 1–11.

[42] N. Buannic, P. Cartraud, G. L'Hostis, Homogénéisation de structures ou matériaux constitués de poutres, Colloque national en calcul des structures, Giens, France (1999).

[43] D. D. Tjahjanto, A. Tyrberg, J. Mullins, Bending Mechanics of Cable Cores and Fillers in a Dynamic Submarine Cable, volume 38, Trondheim, Norway.

[44] W. Jiang, M. Warby, J. Henshall, Statically indeterminate contacts in axially loaded wire strand, European Journal of Mechanics - A/Solids 27 (2008) 69–78.

- Helical strands analysis is addressed rigorously with homogenization theory
- Strand response is non-linear due to contact interactions between its components
- Different models with solid and beam finite elements are used
- Numerical results are compared to those coming from analytical models